Available online at www.sciencedirect.com
ScienceDirect
Trans. Nonferrous Met. Soc. China 32(2022) 2164−2176
Transactions of Nonferrous Metals Society of China
www.tnmsc.cn

Base material location dependence of corrosion response in friction-stir-welded dissimilar 2024-to-5083 aluminum alloy joints

Peng-liang NIU[1,2,3], Wen-ya LI[2], Yu-hua CHEN[1], Qi-peng LIU[1], Dao-lun CHEN[3]

1. National Defense Key Disciplines Laboratory of Light Alloy Processing Science and Technology, School of Aeronautical Manufacturing Engineering, Nanchang Hangkong University, Nanchang 330063, China;
2. Shaanxi Key Laboratory of Friction Welding Technologies, State Key Laboratory of Solidification Processing, Northwestern Polytechnical University, Xi'an 710072, China;
3. Department of Mechanical and Industrial Engineering, Toronto Metropolitan University, Toronto M5B2K3, Canada

Received 6 July 2021; accepted 8 April 2022

Abstract: The effects of the base material (BM) location on the mechanical properties and the exfoliation corrosion performance of friction-stir-welded (FSWed) dissimilar 2024-to-5083 aluminum alloy joints were investigated. Scanning electron microscopy (SEM), electron backscatter diffraction (EBSD), transmission electron microscopy (TEM), tensile tests and electrochemical experiments were conducted. The results revealed that the BM location had little effect on the tensile properties of the joints. The grain orientation spread (GOS) value of 2024 alloy side was lower than that of 5083 alloy side. Intergranular corrosion occurred mainly on the 2024 alloy side, while the grain interior of the 5083 alloy side was corroded due to the higher GOS value and dislocation density. The FSWed dissimilar joints with a superior exfoliation corrosion resistance could be achieved when the 5083 aluminum alloy with better corrosion performance was positioned on the retreating side.

Key words: friction stir welding; dissimilar aluminum alloys; microstructure; mechanical properties; exfoliation corrosion

1 Introduction

Age hardenable aluminum alloys, 2xxx series, are widely utilized in the aerospace industry as their structural weight reduction [1]. 2024 aluminum alloy possesses moderate yield strength and good damage tolerance [2]. In this alloy, pitting and galvanic corrosion are main corrosion forms [3,4]. 5083 aluminum alloy has good balance between light weight and corrosion resistance [5,6]. It was reported that anodic Al−Mg and Al (Mg−Si) phases in the vicinity of cathodic Al (Mn, Fe, Cr) intermetallic compounds (IMCs) made 5083 alloy susceptible to localized corrosion in the forms of pitting, intergranular cracking and stress corrosion cracking (SCC) [7,8].

Friction stir welding (FSW), a solid-state welding process, provides a feasible solution to overcome the problem introduced by fusion welding techniques. Severe plastic deformation at high temperatures occurred in the base material (BM) during FSW process, leading to a joint with very inhomogeneous microstructures, i.e., stir zone (SZ), thermo-mechanically affected zone (TMAZ), heat-affected zone (HAZ) and BM [9−15]. Due to the heterogeneity of a friction-stir-welded (FSWed) joint, various corrosion susceptibilities occurred in

Corresponding author: Wen-ya LI, Tel: +86-29-88495226, Fax: +86-29-88492642, E-mail: liwy@nwpu.edu.cn;
Dao-lun CHEN, Tel: +416-979-5000 ext 6487, Fax: +416-979-5265, E-mail: dchen@ryerson.ca
DOI: 10.1016/S1003-6326(22)65938-7

sub-regions of the joint, especially for the FSWed dissimilar joints [16]. JARIYABOON et al [17] reported that SZ was easy to be attacked by intergranular corrosion (IGC). KHOSHNAW and GARDI [18] reported that the exfoliation corrosion extent of 2024-SZ increased and that of 7075-SZ decreased with increasing the aging time. DONATUS et al [19] found that corrosion initiated at the interface of 6082 and 5083 alloys, where galvanic reaction was easy to form. SHEN et al [20] reported that the corrosion resistance of SZ was higher than that of the two BMs for the FSWed 5083-to-6082 joint. It was reported that the elongated grains would impede the corrosion penetration perpendicular to the major deformation direction when compared with the small grains [21,22]. ZANDER et al [23] reported that the penetration depth of an intergranular corrosion was significantly affected by the grain shape and orientation. Overaging was an efficient way to reduce the IGC susceptibility due to the coarsening of the grain boundaries and grain interior [24]. It was evident that grains with a high level of dislocation density made them more susceptible to preferential attack at grain boundaries [3]. A lot of efforts have been made to reduce the rate of corrosion, which can significantly affect the lifetime of structural components. Many issues regarding corrosion of FSWed dissimilar aluminum alloys are still unclear.

The main objective of this study is to investigate the inhomogeneous corrosion behavior of FSWed 2024-to-5083 aluminum alloy joints with a combination of higher mechanical strength on the one side and superior corrosion performance on the other side. The joints were immersed in an EXCO solution and electrochemical measurements were simultaneously conducted on BMs, HAZs and SZs. The corrosion mechanisms on both sides were clarified based on the electrochemical results, microstructure degradation of the corroded zones (BMs, HAZs and SZs) and deformation within individual grains measured by electron backscatter diffraction (EBSD). Moreover, the effects of BM location on the material flow, microstructure evolution and tensile properties of the joints were evaluated. The results obtained in this study will pave the way for promoting the reliable applications of FSWed joints.

2 Experimental

2.1 Welding experiments

2024-T351 and 5083-H112 (retaining the effective strain hardening applied by the hot work) aluminum alloy plates of dimensions of 6.35 mm × 200 mm × 100 (T×L×W) were FSWed with a commercial FSW machine (FSW-RL31−010, Beijing FSW Technology Co., Ltd., China) parallel to the plate rolling direction (RD). A rotational rate of 600 r/min and welding speeds of 150 and 250 mm/min were selected. The schematic diagram of welding process and the tool profile are shown in Fig. 1. The tool was characterized by a threaded pin having 5.9 mm in diameter (pin diameter, PD) and 6.0 mm in length (pin length, PL) and a concave shoulder of 15.0 mm in diameter (shoulder diameter, SD). The tilted angle of rotating tool was set to be 2.5° and the plunge depth was 0.2 mm. Two types of joints were made: 2024-T351/5083-H112 (with 2024-T351 alloy positioned on the advancing side (AS), referred to as 25-joint), and 5083-H112/2024-T351 (with 2024-T351 alloy placed on the retreating side (RS), labelled as 52-joint).

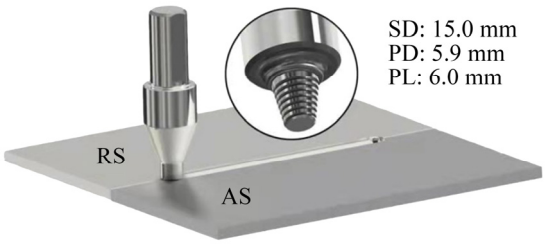

Fig. 1 Schematic diagram of welding process and tool profile

2.2 Corrosion tests

An EXCO solution (4 mol/L NaCl, 0.5 mol/L KNO_3 and 0.1 mol/L HNO_3) was selected as the exfoliation corrosion solution according to the ASTM G34 when the corrosion tests were conducted. Electrochemical experiments were conducted on the FSWed joints via a three-electrode system. A saturated calomel electrode (SCE) with Luggin capillary, a large platinum sheet, and a measured zone with the area of 1 cm^2 were served as a reference electrode (RE), counter electrode (CE), and working electrode (WE), respectively. Open circuit potential (OCP) measurements were

performed on the top surface of SZs, HAZs and BMs of the welded joints. Electrochemical impedance spectroscopy (EIS) tests were carried out in the range of 0.01 Hz to 100 kHz with a 5 mV AC signal amplitude at the OCP. At a scan rate of 0.5 mV/s, the polarization tests were performed when a potential range was from 0.25 V (vs open circuit) to 1.6 V (vs reference electrode).

2.3 Microstructural characterization

Optical microscope (OM) was utilized to characterize the macrostructure of the welded joints. Electron backscatter diffraction (EBSD) was employed to measure the grain morphology and grain orientation spread (GOS) maps of the SZs and BMs. Scanning electron microscopy (SEM) was conducted to get the microstructural evolution of the corrosion damaged zones across the joint cross-section including BM, HAZ and SZ. Transmission electron microscopy (TEM) was used to observe the dislocation structures and precipitates state of the 5083 aluminum alloy SZ and HAZ.

3 Results and discussion

3.1 Weld formation and tensile properties

The weld surface of the joints made with different welding parameters at different BM positions is shown in Fig. 2. It is seen that the sound weld appearance was fabricated at the rotation rate of 600 r/min and welding speeds of 150 and 250 mm/min when 2024 aluminum was placed on the AS. As presented in Fig. 3, the BM location almost has no effect on the tensile properties of joints when the same welding parameters were used. All the tensile samples were fractured at the HAZ of 5083 aluminum alloy side where strain localizations could be detected. Therefore, the tensile properties of the global joint are dominantly determined by 5083 aluminum alloy side.

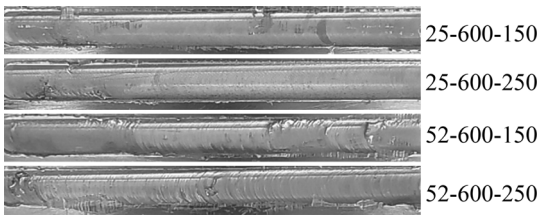

Fig. 2 Weld surface morphology of FSWed joints with different welding parameters at different BM locations

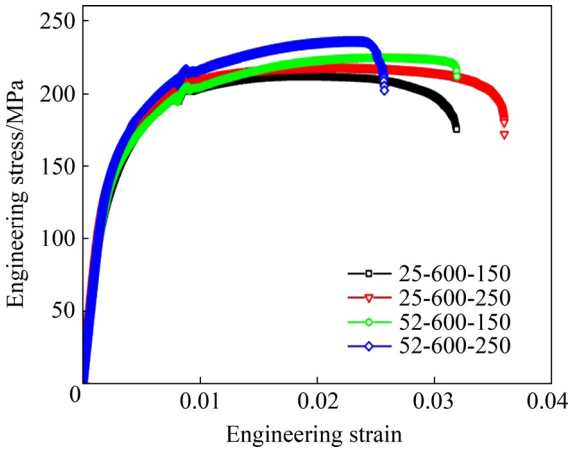

Fig. 3 Engineering stress−strain curves of 25- and 52-joint at different welding parameters

3.2 Macro- and micro-structures

The cross-sectional macrostructures of the 25-joint and 52-joint are shown in Figs. 4(a) and (b), respectively. It is widely believed that the plastic metal of the SZ top horizontally flows from RS to AS. Thus, under the effect of tool shoulder the top of the SZ almost consisted of the BM in RS, especially for the 25-joint, which will in turn significantly affect the corrosion perfomance of the weld top surface. For the middle and lower parts of SZ, the plastic metal, driven by the tool pin with screw went through the initial butt line from AS to RS. Therefore, the top of the SZ predominantly consisted of the BM which was positioned on the RS, and the middle and bottom of the SZ were mainly composed of the BM placed on the AS, as indicated by the vertical dashed line in Fig. 4. This suggests that the BM configuration or positioning has a significant effect on the microstructure and composition of the FSWed joint. The EBSD analysis zones are marked by the red rectangles and

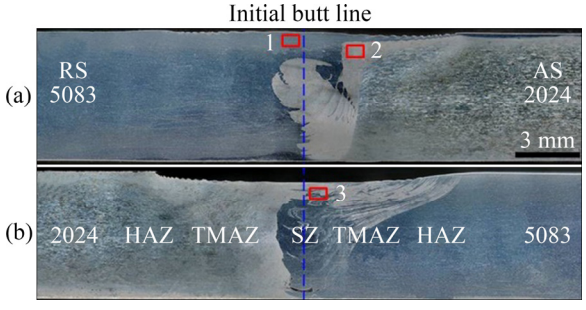

Fig. 4 Cross-sectional macrostructures of 2024-5083 dissimilar aluminum alloy joints: (a) 25-joint; (b) 52-joint

their results will be presented in the following section.

Figure 5 shows the EBSD results of 2024- and 5083-BMs. As shown in Figs. 5(a) and (b), the grains were colored according to their crystallographic orientations. The grain size and shape have been described in the former paper [25]. Here, the GOS maps are presented. It can be observed from Figs. 5(c) and (d) that the GOS value determined from the EBSD measurements of 5083-BM is much higher than that of 2024-BM, which should be attributed to the highly deformed grains deriving from the rolling process. The GOS gives a quantitative description of the crystallographic orientation gradients within individual grains, which affects their corrosion resistance [26,27].

Figure 6 illustrates the grain orientation and GOS maps of the 25-SZ and 52-SZ at the top as indicated in Fig. 4, where corrosion tests were conducted. The EBSD measurement zones were located in the shoulder affected zone (SAZ), where the heat and severe plastic strain were mainly introduced by the tool shoulder during welding. It is of interest to note from Figs. 6(a, d) that an abnormally big grain with a high GOS value appears in the 25-SZ of 2024 side (Position 1 in Fig. 4), indicating the occurrence of incompletely dynamic recrystallization. The GOS value distribution of different zones is presented in Fig. 7. The GOS values lower than ·0.6° are dominant in 5083-SZ, 2024-SZ and 52-SZ. The most GOS values of 2024-BM is in the range of 0.3°−1.1°. Because of the higher plastic deformation induced during the rolling process, the GOS value of 5083-BM within the scope of 2°−3.2° is much higher than that in other zones. Moreover, the GOS value of different grains makes a big difference, which will affect the corrosion response of individual grains.

3.3 Corrosion performance response

OCP values of the SZs, HAZs and BMs of 2024 and 5083 surfaces immersed in the EXCO solution are shown in Figs. 8(a) and (b), respectively. It is convinced that the kinds of intermetallic particles play a very important role in the OCP value of a material, which will in turn affect its corrosion performance [28]. The OCP value of 2024 side is much higher than that of 5083 side. It is seen from Fig. 8(a) that the OCP

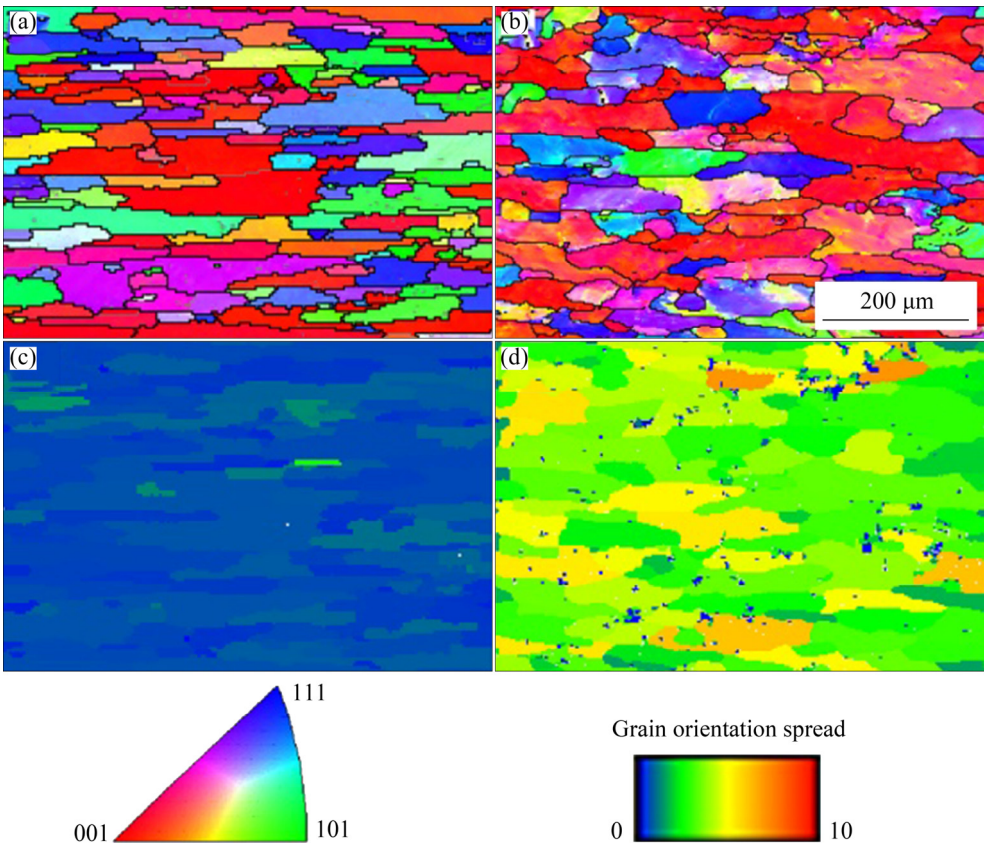

Fig. 5 EBSD orientation maps (a, b) and grain orientation spread maps (c, d) of BMs: (a, c) 2024-BM; (b, d) 5083-BM

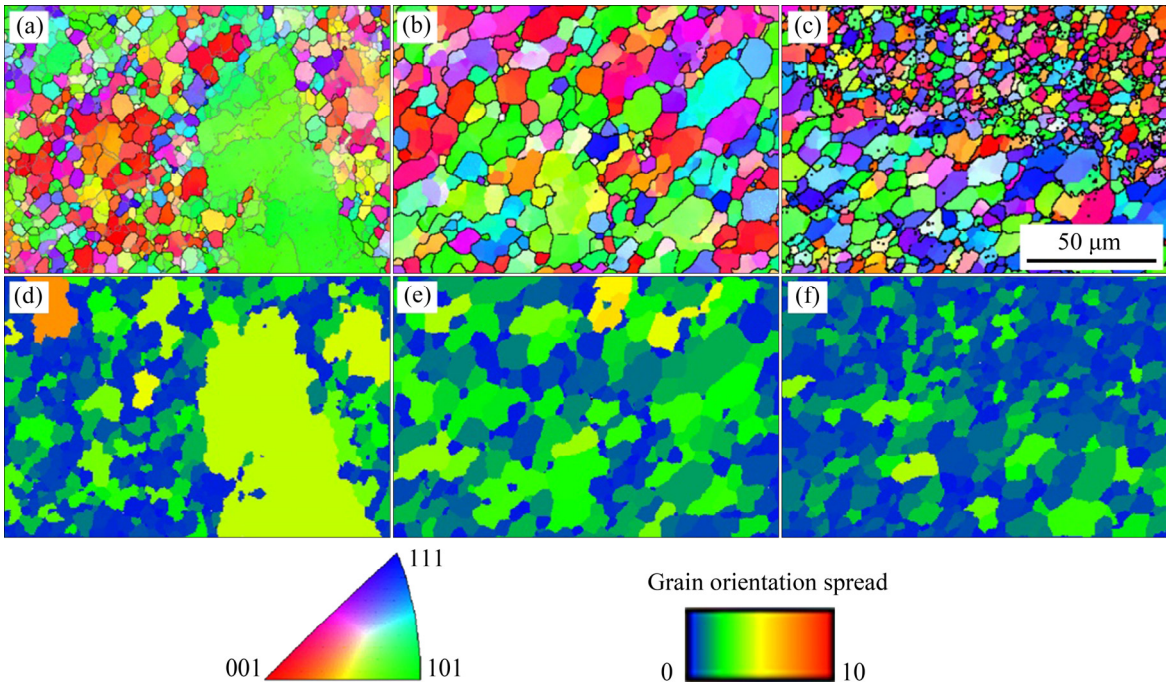

Fig. 6 EBSD orientation maps (a, b, c) and grain orientation spread maps (d, e, f) of SZ: (a, d) 25-SZ (2024 side); (b, e) 25-SZ (5083 side); (c, f) 52-SZ (2024/5083 interface)

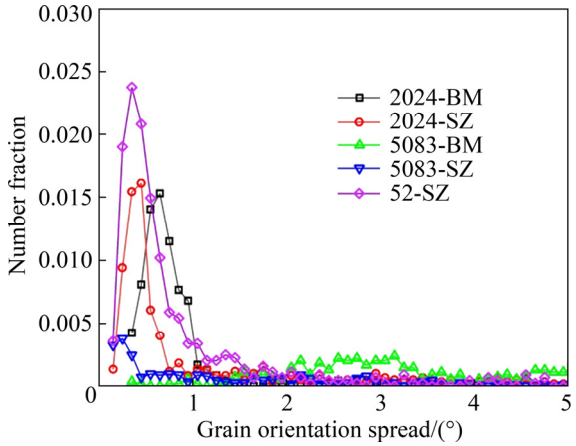

Fig. 7 GOS value distribution of different zones of joint cross-section

value of 2024-BM is the highest and that of the SZ is the lowest. On the 2024 side, the OCP values of different zones make a big difference (Fig. 8(a)), while those appear to be constant on the 5083 side (Fig. 8(b)). This would be attributed to the more sensitivity to the heat effect of heat-treatable 2024 aluminum alloy because of the evolution of precipitates during welding. It is known that the content and distribution of precipitates have a significant influence on the corrosion resistance of a material. Moreover, the OCP value of SZ is closer to that of 5083-BM rather than 2024-BM, which is

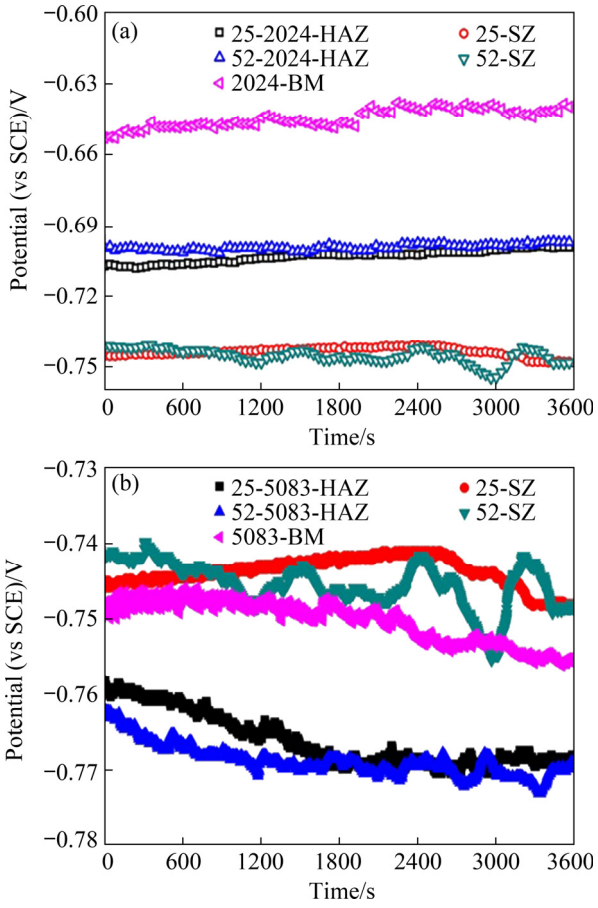

Fig. 8 Open circuit potential of various zones in 25- and 52-joint as function of time: (a) AA2024 side; (b) AA5083 side

also different from the results of our previous study on the FSWed 2024-to-7075 joints, where the OCP value of SZ was closer to that of the BM positioned in the RS [29].

The polarization curves from the 25-joint and 52-joint cross-sections immersed in the EXCO solution are presented in Fig. 9. The anodic and cathodic reactions are asymmetric. Passivation is absent in all of these measured zones throughout the scanned potential range. The corrosion potential (φ_{corr}) and current densities (J_{corr}) based on the Tafel fitting of polarization curves are listed in Table 1. The φ_{corr} values of different zones on the 2024 side are higher than those on the 5083 side. Also, the φ_{corr} values of SZs are similar to those of 5083 side. The composition of precipitates or intermetallics plays an important role in the φ_{corr} values, which can be measured by Kelvin probe force microscopy (SKPEM) [6]. The main precipitates in 5083-BM were identified as Al_3Mg_2 and Mg_2Si [7,8]. It was unreliable to judge the corrosion performance of a material by φ_{corr} value, which could only provide a tendency or possibility of corrosion [30]. The J_{corr}

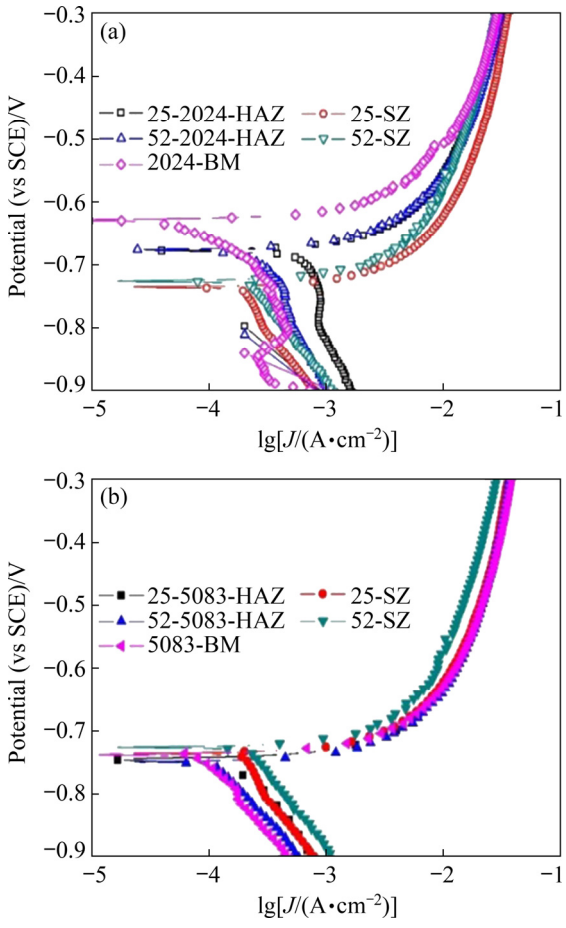

Fig. 9 Polarization curves of various zones in 25- and 52-joint: (a) 2024 side; (b) 5083 side

Table 1 Electrochemical parameters in different zones of FSWed joints calculated from Tafel polarization curves

Location	φ_{corr}(vs SCE)/mV	J_{corr}/(10^{-5} A·cm^{-2})
2024-BM	−637.3	8.5
5083-BM	−751.0	12
25-SZ	−736.6	22
52-SZ	−762.6	24
25-2024-HAZ	−680.5	38
52-2024-HAZ	−674.9	17
25-5083-HAZ	−752.3	18
52-5083-HAZ	−760.4	14

values of 2024-HAZs are obviously higher than those of 2024-BM, while the J_{corr} values of 5083-HAZs are slightly higher than those of 5083-BM. Furthermore, the BM position has almost no effect on the φ_{corr} and J_{corr} of SZs.

Electrochemical impedance spectroscopy (EIS) and equivalent circuit diagram of different zones on the 25-joint and 52-joint cross-section are presented in Fig. 10. The fitted circuit constants by using the ZVIEW software are listed in Table 2, where E_1−E_4 and respectively the corresponding errors between the fitted and experimental results in their former columm. And the equivalent circuit is inserted in Fig. 10(a), where R_s and R_p stand for the resistance of EXCO solution and oxide film with a capacitance, respectively, and the equivalent capacitance of the oxide film layer was named as CPE [31]. The fitted results of different zones indicate that the resistances of EXCO solution, R_s, are similar to each other. The polarization resistances of 5083 and 2024-BMs, R_p, are 438.4 and 255.2 Ω·cm^2, respectively. The R_p value of 25-SZ is 269.5 Ω·cm^2, which is ~49% higher than that of 52-SZ. Therefore, it is preferable to position of 5083-BM in the RS, leading to a joint with better exfoliation corrosion performance in the EXCO solution. The location of BMs has almost no effect on the value of R_p. In both joints, the weakest zone for the corrosion resistance is 2024-HAZ.

The Bode plots at the OCPs of BMs, HAZs and SZs on the 25- and 52-joint cross-sections are presented in Fig. 11. It can be seen that the values of $|Z|$ on the 2024 side are almost stable at the beginning and then decrease with increasing frequency. An obvious peak value of $|Z|$ appears on the 5083 side. The $|Z|$ peak value is equal to that of

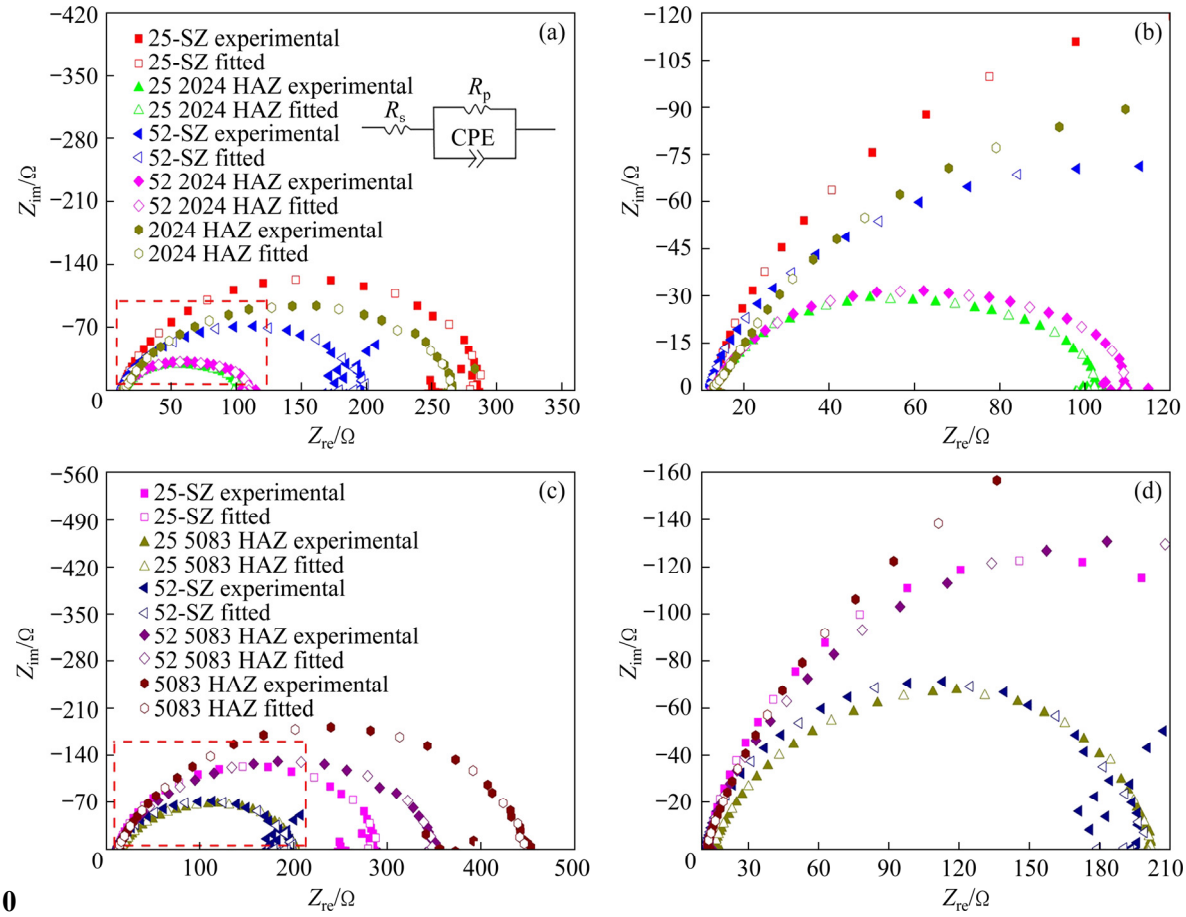

Fig. 10 Electrochemical impedance spectroscopy (EIS) graphs of various zones in 25- and 52-joint: (a) EIS and equivalent circuit diagram on 2024 side; (b) Magnified red dashed box in (a); (c) EIS on 5083 side; (d) Magnified red dashed box in (c)

Table 2 Impedance parameters of equivalent circuit obtained from fitted EIS results of various zones in 25- and 52-joint

Location	R_s/(Ω·cm^2)	E_1/%	R_p/(Ω·cm^2)	E_2/%	C_p/(10^{-5} F·cm^{-2})	E_3/%	n_p	E_4/%
2024-BM	13.17	1.47	255.2	1.15	12.2	4.78	0.79	0.94
5083-BM	12.27	3.00	438.4	1.05	1.82	5.69	0.83	0.86
25-SZ	12.62	1.94	269.5	1.09	1.62[5]	6.69	0.91	0.95
52-SZ	11.49	1.97	180.6	0.95	2.51	6.72	0.84	1.00
25-2024-HAZ	12.15	1.10	90.07	0.83	22.6	4.69	0.75	0.95
52-2024 HAZ	12.13	1.07	97.23	0.88	21.3	4.91	0.76	1.00
25-5083-HAZ	14.66	2.40	186.3	1.07	3.7	7.64	0.77	1.25
52-5083-HAZ	11.84	3.88	326.2	1.51	1.60	9.70	0.83	1.41

time constant. Different time constants correspond to different electrode reactions. Therefore, only one time constant exists in these cases. Generally, the higher the value of $|Z|$ is, the better the corrosion resistance is. It follows that the corrosion resistance of 25-SZ is better than that of 52-SZ.

The phase angle diagrams at the OCPs of different zones in the 25- and 52-joints are displayed in Fig. 12. The lg f vs phase angle curves can be employed to differentiate the small change in time constant. It is confirmed from Fig. 12 that only one time constant exists, which is in accordance with the results of Bode plots. The capacitive reactance response can be identified when the value of phase angle is positive. On the contrary, when the value of phase angle is negative, the impedance

response appears. Therefore, the impedance response is dominant in the corrosion process in this work. The higher the absolute value of phase angle is, the better the corrosion resistance is. It is inferred that the corrosion performance of 5083 side is better than that of 2024 side, and the 2024-HAZ is the weakest. The location of BMs has a significant effect on the corrosion resistance of SZs and 5083-HAZs.

3.4 Microstructure degradation after exfoliation corrosion

Figure 13 shows the typical microstructure morphologies of different zones across the 25-joint after immersing in the EXCO solution. It is seen from the 2024 side that severe intergranular corrosion appears along the grain boundaries. As listed in Table 3, EDS results indicate that the Cu-rich and Mn-rich big intermetallic particles in the 2024-SZ are also present. Chloridion derived from the EXCO solution was detected in the corrosion products of 2024-HAZ. And sodium originated from the EXCO solution was also detected in the 5083-HAZ. The grains of 5083 side were corroded rather than grain boundaries, which makes a big difference from the 2024 side. This should be attributed to a lower number of precipitates in the 5083 side. Therefore, it is harder for the grain boundaries of 5083 to be corroded. It was reported by ZANDER et al [23] that the shape and orientation of grains had a significant effect on the intergranular corrosion behavior, which was also demonstrated by other researchers [21,22]. Moreover, LUO et al [3] considered that the grains with higher dislocation densities stored higher energies, which in turn were more vulnerable to be corroded. It can be seen from Figs. 5 and 6 that there exist almost no differences in the grain texture of BMs and SZs, while the GOS values and the subsequent dislocation densities (the higher the

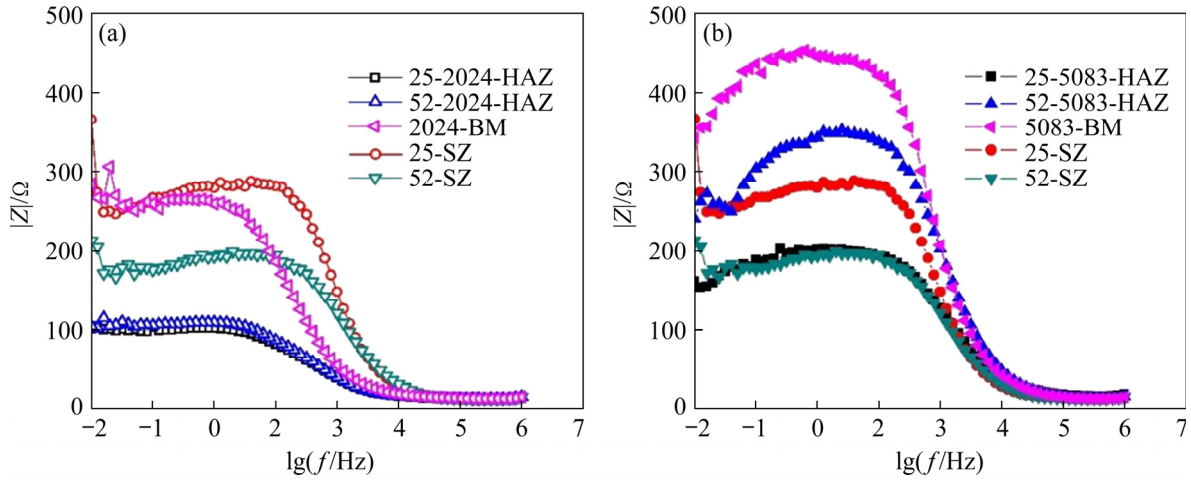

Fig. 11 Bode plots of various zones in 25- and 52-joint in EXCO solution: (a) 2024 side; (b) 5083 side

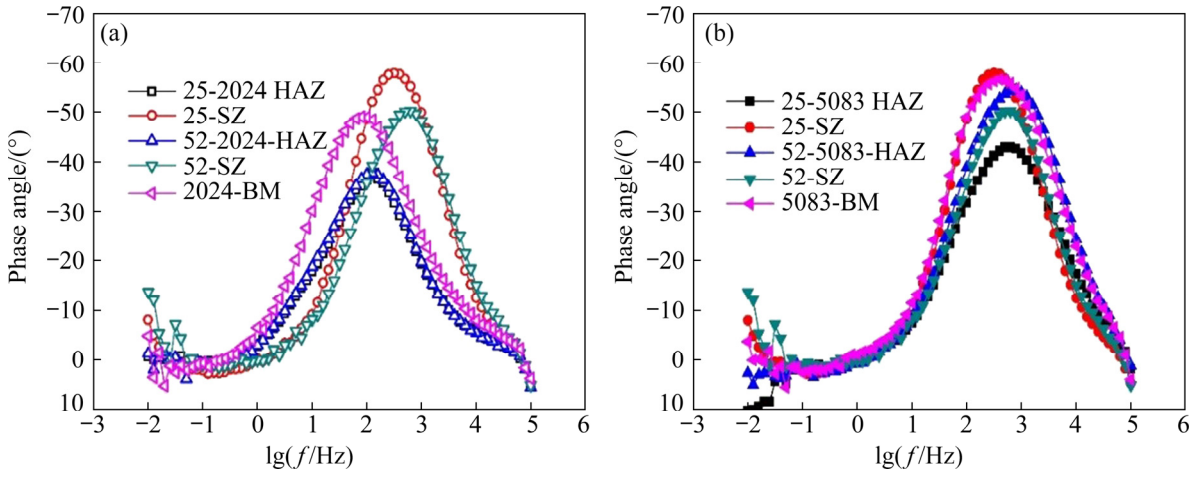

Fig. 12 Phase angles of various zones in 25- and 52-joint in EXCO solution: (a) 2024 side; (b) 5083 side

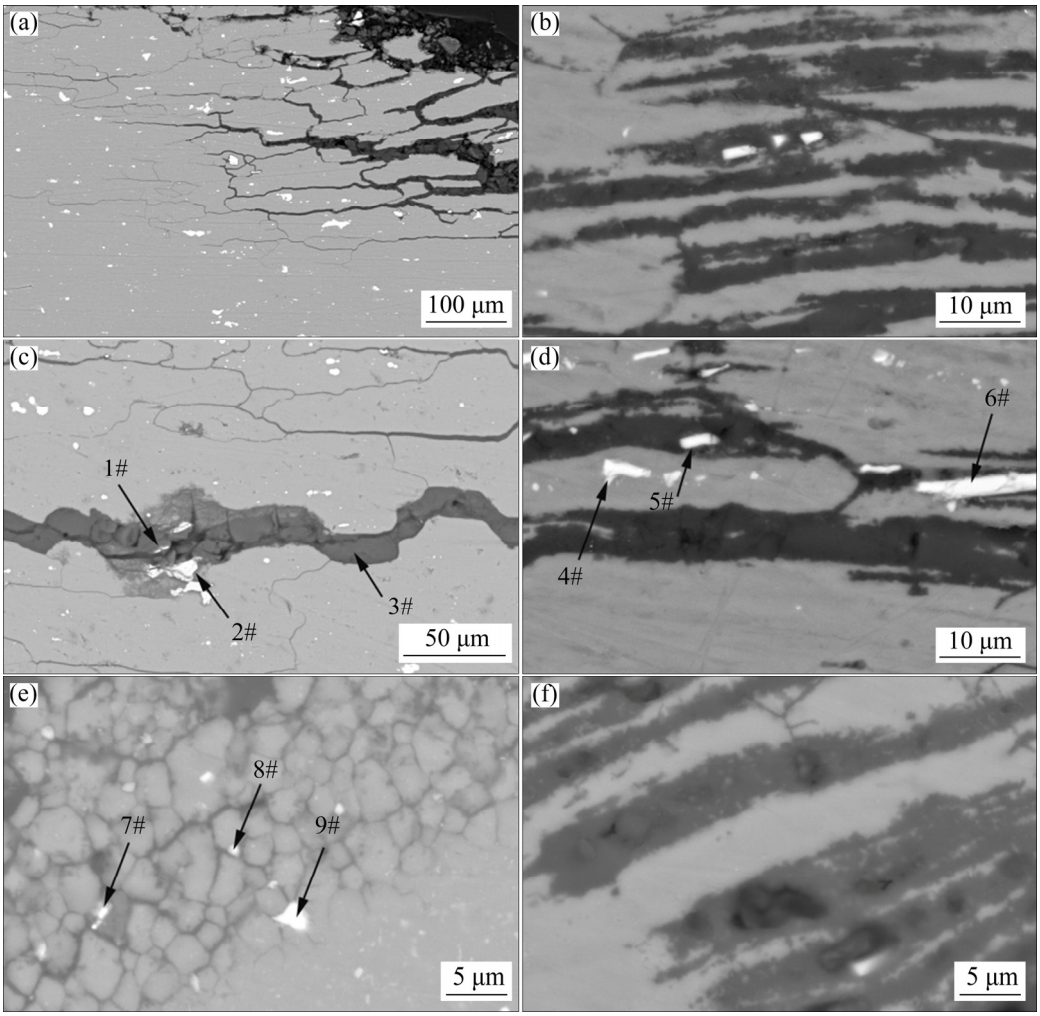

Fig. 13 Corrosion morphologies of different zones of 25-joint: (a) 2024-BM; (b) 5083-BM; (c) 2024-HAZ; (d) 5083-HAZ; (e) 2024-SZ; (f) 5083-SZ

Table 3 EDS results of composition at positions marked in Fig. 13 (wt.%)

No.	Al	Fe	Cu	Mg	Mn	Cr	Si	Cl	Na
1#	45.6	4.3	48.2	−	1.3	−	−	0.6	−
2#	61.9	14.6	13.8	−	9.7	−	−	−	−
3#	94.1	−	1.1	0.8	−	−	1.1	2.9	−
4#	77	20	0.7	−	0.7	1.6	−	−	−
5#	71.5	21.8	0.6	−	0.9	3.9	−	−	1.3
6#	70.9	24.1	0.7	−	0.8	3.4	−	−	−
7#	71.9	−	27.8	−	0.3	−	−	−	−
8#	79.9	2.3	16.8	−	1	−	−	−	−
9#	55.1	−	33.2	11.6	0.1	−	−	−	−

GOS values are, the higher the dislocation densities are) of 5083-BM and 5083-SZ are higher than those of 2024, especially in the case of BMs.

Figure 14 shows the TEM images of 5083 SZ and 5083-HAZ. It can be observed that large numbers of dislocation structures appear near grain boundaries in both 5083-SZ and 5083-HAZ. This should be attributed to the incomplete dynamic recrystallization for 5083-SZ and partial recovery for 5083-HAZ. The precipitates consisted of Al, Mg, Si, Cr, and Fe, as reported in our previous work [32]. The dislocation structures and precipitates state of 2024 aluminum alloy have been identified [33]. Under considerations of the above-mentioned factors, corrosion occurs mainly in the form of intergranular corrosion (IGC) on the 2024 side because of the appearance of consecutive grain boundaries precipitates and precipitation-free zones [34,35] and in the form of grain interior attack on the 5083 side, and pitting takes place at the precipitates or intermetallic particles on both sides, as summarized schematically in Fig. 15.

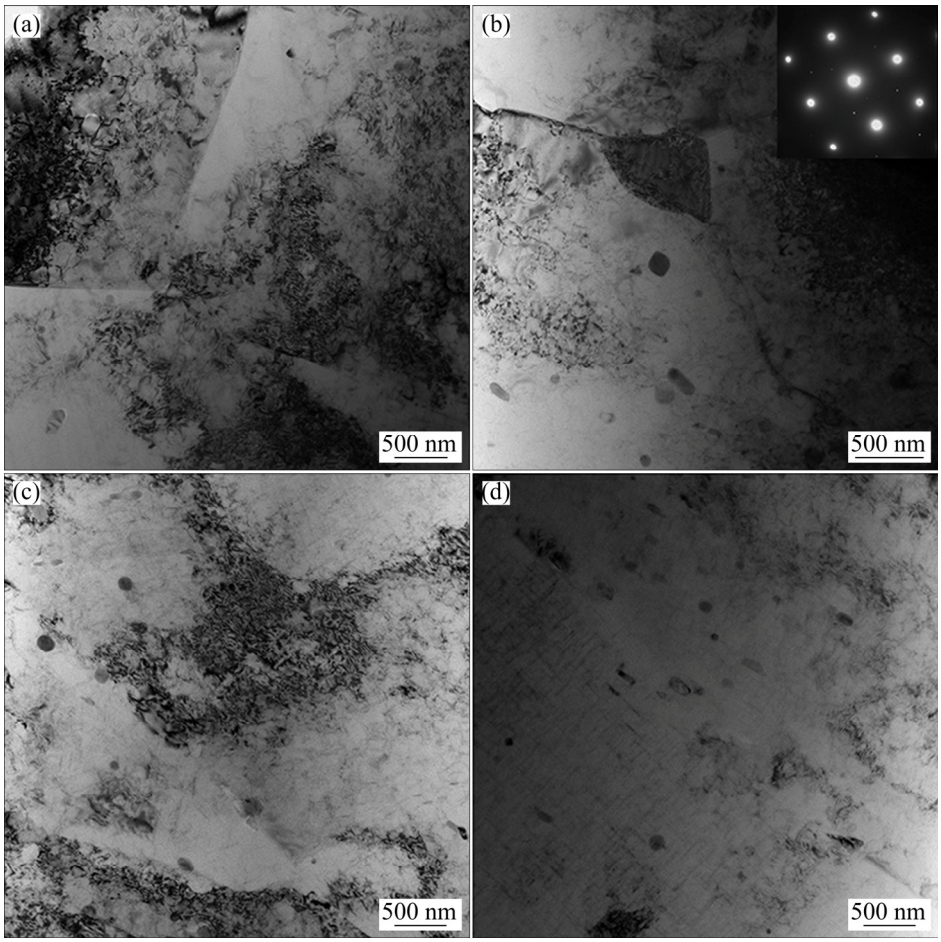

Fig. 14 TEM bright field images of 5083 aluminum side, and associated ⟨001⟩ Al diffraction pattern: (a, b) 5083-SZ; (c, d) 5083-HAZ

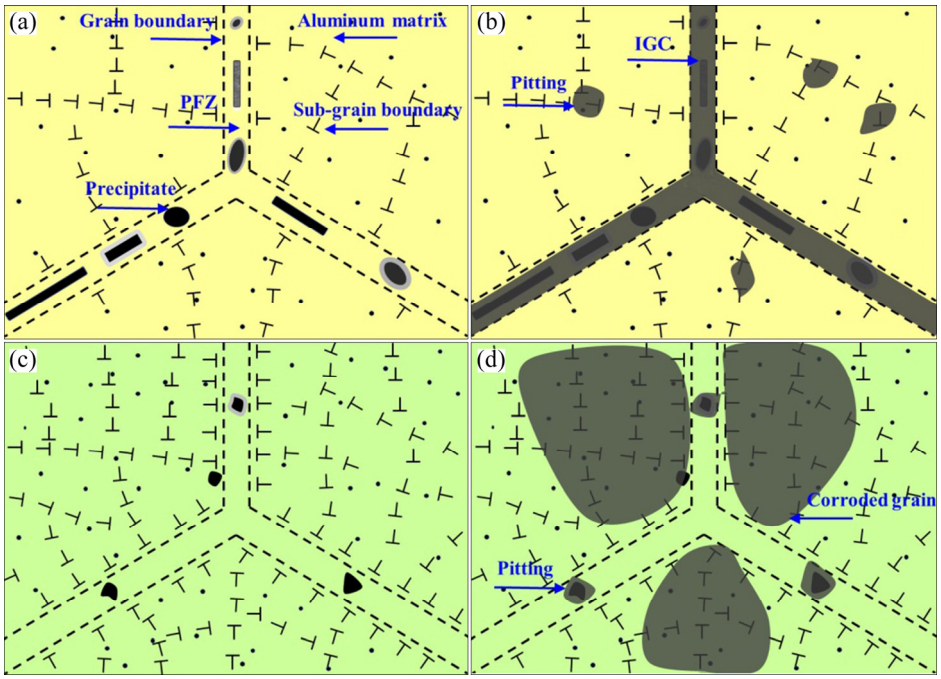

Fig. 15 Schematic diagrams showing corrosion mechanisms of joint: (a) 2024 side of as-welded joint; (b) 2024 side of corroded joint; (c) 5083 side of as-welded joint; (d) 5083 side of corroded joint

4 Conclusions

(1) The GOS value of 2024-BM was much smaller than that of 5083-BM, and the GOS value of 2024-SZ was also smaller than that of 5083-SZ. The BM location has little effect on the tensile properties of the joints.

(2) The corrosion current density (J_{corr}) of 2024-HAZ was obviously higher than that of 2024-BM, and the J_{corr} of 5083-HAZ slightly increased when compared with that of 5083-BM.

(3) The polarization resistance (R_p) value of 25-SZ was observed to be ~49% higher than that of 52-SZ, suggesting that the FSWed joints with a higher corrosion resistance could be fabricated when the 5083 aluminum alloy with better corrosion performance was positioned on the RS. IGC predominantly occurred on the 2024 side and the grain interior of the 5083 side was severely corroded.

Acknowledgments

The authors would like to gratefully acknowledge the financial supports from the National Natural Science Foundation of China (No. 52105357), the Natural Sciences and Engineering Research Council of Canada (NSERC) in the form of international research collaboration, the Natural Science Foundation for Youth of Jiangxi Education Department, China (No. DA202003181), the Foundation of National Defense Key Disciplines Laboratory of Light Alloy Processing Science and Technology of China (No. EG202103420), as well as the Doctor Starting Foundation of Nanchang Hangkong University, China (No. EA202003208). The authors would also like to thank Q LI, A. MACHIN, J. AMANKRAH and R. CHURAMAN for easy access to the laboratory facilities of Toronto Metropolitan University and their assistance in the experiments.

References

[1] ZHAO Y L, YANG Z Q, ZHANG Z, SU G Y, MA X L. Double-peak age strengthening of cold-worked 2024 aluminum alloy [J]. Acta Materialia, 2013, 61: 1624−1638.

[2] TIAMIYU A A, BADMOS A Y, ODESHI A G, SZPUNAR J A. The influence of temper condition on adiabatic shear failure of AA 2024 aluminum alloy [J]. Materials Science and Engineering A, 2017, 708: 492−502.

[3] LUO C, ZHOU X, THOMPSON G E, HUGHES A E. Observations of intergranular corrosion in AA2024-T351: The influence of grain stored energy [J]. Corrosion Science, 2012, 61: 35−44.

[4] BOAG A, HUGHES A E, GLENN A M, MUSTER T H, MCCULLOCH D. Corrosion of AA2024-T3. Part I: Localised corrosion of isolated IM particles [J]. Corrosion Science, 2011, 53: 17−26.

[5] GUNGOR B, KALUC E, TABAN E, SIK A. Mechanical, fatigue and microstructural properties of friction stir welded 5083-H111 and 6082-T651 aluminum alloys [J]. Materials & Design, 2014, 56: 84−90.

[6] YASAKAU K A, ZHELUDKEVICH M L, LAMAKA S V, FERREIRA M G S. Role of intermetallic phases in localized corrosion of AA5083 [J]. Electrochimica Acta, 2007, 52: 7651−7659.

[7] LYNDON J A, GUPTA R K, GIBSON M A, BIRBILIS N. Electrochemical behaviour of the β-phase intermetallic (Mg_2Al_3) as a function of pH as relevant to corrosion of aluminium–magnesium alloys [J]. Corrosion Science, 2013, 70: 290−293.

[8] DUPUY L, BLANDIN J J. Damage sensitivity in a commercial Al alloy processed by equal channel angular extrusion [J]. Acta Materialia, 2002, 50: 3253−3266.

[9] MA Zong-yi, FENG Ai-han, CHEN Dao-lun, SHEN Jun. Recent advances in friction stir welding/processing of aluminum alloys: Microstructural evolution and mechanical properties [J]. Critical Reviews in Solid State and Materials Sciences, 2018, 43: 269−333.

[10] LIU Xiao-chao, ZHEN Yun-qian, SUN Yu-feng, SHEN Zhi-kang, CHEN Hai-yan, GUO Wei, LI Wen-ya. Local inhomogeneity of mechanical properties in stir zone of friction stir welded AA1050 aluminum alloy [J]. Transactions of Nonferrous Metals Society of China, 2020, 30: 2369−2380.

[11] XU Wei-feng, MA Jun, WANG Miao, LU Hong-jian, LUO Yu-xuan. Effect of cooling conditions on corrosion resistance of friction stir welded 2219-T62 aluminum alloy thick plate joint [J]. Transactions of Nonferrous Metals Society of China, 2020, 30: 1491−1499.

[12] RAJENDRAN C, SRINIVASAN K, BALASUBRAMANIAN V, BALAJI H, SELVARAJ P. Effect of tool tilt angle on strength and microstructural characteristics of friction stir welded lap joints of AA2014-T6 aluminum alloy [J]. Transactions of Nonferrous Metals Society of China, 2019, 29: 1824−1835.

[13] XU Nan, CHEN Lei, GU Bo-kun, REN Zi-ke, SONG Qi-ning, BAO Ye-feng. Heterogeneous structure-induced strength and ductility synergy of α-brass subjected to rapid cooling friction stir welding [J]. Transactions of Nonferrous Metals Society of China, 2021, 31: 3785−3799.

[14] YANG Xia-wei, FENG Wu-yuan, LI Wen-ya, DONG Xiu-rong, XU Ya-xin, CHU Qiang, YAO Shuo-tian. Microstructure and properties of probeless friction stir spot welding of AZ31 magnesium alloy joints [J]. Transactions of Nonferrous Metals Society of China, 2019, 29: 2300−2309.

[15] MENG Qiang, LIU Yang, KANG Ju, FU Rui-dong, GUO Xiao-yan, LI Yi-jun. Effect of precipitate evolution on corrosion behavior of friction stir welded joints of AA2060-T8 alloy [J]. Transactions of Nonferrous Metals Society of China, 2019, 29: 701−709.

[16] DIXIT M, MISHRA R S, SANKARAN K K. Structure-property correlations in Al 7050 and Al 7055 high-strength aluminum alloys [J]. Materials Science and Engineering A, 2008, 478: 163−172.

[17] JARIYABOON M, DAVENPORT A J, AMBAT R, CONNOLLY B J, WILLIAMS S W, PRICE D A. Corrosion of a dissimilar friction stir weld joining aluminium alloys AA2024 and AA7010 [J]. Corrosion Engineering, Science and Technology, 2006, 41: 135−142.

[18] KHOSHNAW F M, GARDI R H. Effect of aging time and temperature on exfoliation corrosion of aluminum alloys 2024-T3 and 7075-T6 [J]. Materials and Corrosion, 2007, 58: 345−347.

[19] DONATUS U, THOMPSON G E, ZHOU X, WANG J J, CASSELL A, BEAMISH K. Corrosion susceptibility of dissimilar friction stir welds of AA5083 and AA6082 alloys [J]. Materials Characterization, 2015, 107: 85−97.

[20] SHEN C B, CHEN Y, GE J P. Comparison of the electrochemical behaviors among 5083/6082 friction stir welding dissimilar weld and parent materials [J]. Advanced Materials Research, 2010, 139/140/141: 299−302.

[21] HUANG Yuan-chun, LI Yin, XIAO Zheng-bin, LIU Yu, HUANG Yu-tian, REN Xian-wen. Effect of homogenization on the corrosion behavior of 5083-H321 aluminum alloy [J]. Journal of Alloys and Compounds, 2016, 673: 73−79.

[22] JAIN S, HUDSON J L, SCULLY J R. Effects of constituent particles and sensitization on surface spreading of intergranular corrosion on a sensitized AA5083 alloy [J]. Electrochimica Acta, 2013, 108: 253−264.

[23] ZANDER D, SCHNATTERER C, ALTENBACH C, CHAINEUX V. Microstructural impact on intergranular corrosion and the mechanical properties of industrial drawn 6056 aluminum wires [J]. Materials & Design, 2015, 83: 49−59.

[24] SVENNINGSEN G, LARSEN M H, WALMSLEY J C, NORDLIEN J H, NISANCIOGLU K. Effect of artificial aging on intergranular corrosion of extruded AlMgSi alloy with small Cu content [J]. Corrosion Science, 2006, 48: 1528−1543.

[25] NIU Peng-liang, LI Wen-ya, VAIRIS A, CHEN Dao-lun. Cyclic deformation behavior of friction-stir-welded dissimilar AA5083-to-AA2024 joints: Effect of microstructure and loading history [J]. Materials Science and Engineering A, 2019, 744: 145−153.

[26] HADADZADEH A, MOKDAD F, WELLS M A, CHEN D L. A new grain orientation spread approach to analyze the dynamic recrystallization behavior of a cast-homogenized Mg−Zn−Zr alloy using electron backscattered diffraction [J]. Materials Science and Engineering A, 2018, 709: 285−289.

[27] VIGNAL V, BA D, ZHANG H, HERBST F, LE MANCHET S L. Influence of the grain orientation spread on the pitting corrosion resistance of duplex stainless steels using electron backscatter diffraction and critical pitting temperature test at the microscale [J]. Corrosion Science, 2013, 68: 275−278.

[28] DAVOODI A, ESFAHANI Z, SARVGHAD M., Microstructure and corrosion characterization of the interfacial region in dissimilar friction stir welded AA5083 to AA7023 [J]. Corrosion Science, 2016, 107: 133−144.

[29] NIU Peng-liang, LI Wen-ya, LI Na, XU Ya-xin, CHEN Dao-lun. Exfoliation corrosion of friction stir welded dissimilar 2024-to-7075 aluminum alloys [J]. Materials Characterization, 2019, 147: 93−100.

[30] CVIJOVIĆ Z, RADENKOVIĆ G. Microstructure and pitting corrosion resistance of annealed duplex stainless steel [J]. Corrosion Science, 2006, 48: 3887−3906.

[31] de ASSIS S L, WOLYNEC S, COSTA I. Corrosion characterization of titanium alloys by electrochemical techniques [J]. Electrochimica Acta, 2006, 51: 1815−1819.

[32] NIU Peng-liang, LI Wen-ya, CHEN Yu-hua, LIU Fen-cheng, GONG Jie, CHEN Dao-lun. Cyclic hardening behavior and deformation mechanisms of friction-stir-welded dissimilar AA5083-to-AA2024 joints with heterogeneous microstructures [J]. Materials Characterization, 2021, 181: 111465.

[33] NIU Peng-liang, LI Wen-ya, YANG Cheng-gang, CHEN Yu-hua, CHEN Dao-lun. Low cycle fatigue properties of friction stir welded dissimilar 2024-to-7075 aluminum alloy joints [J]. Materials Science and Engineering A, 2022, 832: 142423.

[34] ZUO Jin-rong, HOU Long-gang, SHI Jin-tao, CUI Hua, ZHUANG Lin-zhong, ZHANG Ji-shan. Enhanced plasticity and corrosion resistance of high strength Al−Zn−Mg−Cu alloy processed by an improved thermomechanical processing [J]. Journal of Alloys and Compounds, 2017, 716: 220−230.

[35] WANG Zhi-xiu, CHEN Peng, LI Hai, FANG Bi-jun, SONG Ren-guo, ZHENG Zi-qiao. The intergranular corrosion susceptibility of 2024 Al alloy during re-ageing after solution treating and cold-rolling [J]. Corrosion Science, 2017, 114: 156−168.

母材位置对 2024−5083 异种铝合金搅拌摩擦焊接头腐蚀响应行为的影响

牛鹏亮[1,2,3]，李文亚[2]，陈玉华[1]，刘其鹏[1]，陈道伦[3]

1. 南昌航空大学 航空制造工程学院 轻合金加工技术国防重点学科实验室，南昌 330063；
2. 西北工业大学 凝固技术国家重点实验室 陕西省摩擦焊工程技术重点实验室，西安 710072；
3. Department of Mechanical and Industrial Engineering, Toronto Metropolitan University, Toronto M5B2K3, Canada

摘　要：研究母材放置位置对 2024−5083 铝合金搅拌摩擦焊接头力学性能和剥落腐蚀性能的影响。采用扫描电子显微镜、电子背散射、透射电子显微镜、拉伸试验和电化学腐蚀试验对接头进行分析。结果表明，母材放置位置对接头的拉伸性能影响较小。2024 铝合金侧的晶粒取向分布值低于 5083 铝合金侧。2024 铝合金侧以晶间腐蚀为主，5083 铝合金侧以晶粒内部腐蚀为主，这是由于 5083 铝合金侧的晶粒取向分布值高且位错密度高。当耐腐蚀性好的 5083 铝合金位于后退侧时，接头具有优良的耐腐蚀性能。

关键词：搅拌摩擦焊；异种铝合金；显微组织；力学性能；剥落腐蚀

(Edited by Xiang-qun LI)